State-selective photodissociation dynamics of formaldehyde: Near threshold studies of the H+HCO product channel

W. Scott Hopkins and Hans-Peter Loock[a),b)]
Department of Chemistry, Queen's University, Kingston, Ontario K7L 3N6, Canada

Bríd Cronin, Michael G. D. Nix, Adam L. Devine, Richard N. Dixon, and Michael N. R. Ashfold[a),c)]
School of Chemistry, University of Bristol, Bristol BS8 1TS, United Kingdom

(Received 13 February 2007; accepted 1 June 2007; published online 8 August 2007)

The laser-induced photodissociation of formaldehyde in the wavelength range $309<\lambda<330$ nm has been investigated using H (Rydberg) atom photofragment translational spectroscopy. Photolysis wavelengths corresponding to specific rovibronic transitions in the $\tilde{A}\,^1A_2 \leftarrow \tilde{X}\,^1A_1$ $2_0^1 4_0^3$, $2_0^2 4_0^1$, $2_0^2 4_0^3$, $2_0^3 4_0^1$, and $2_0^1 5_0^1$ bands of H_2CO were studied. The total kinetic energy release spectra so derived can be used to determine partial rotational state population distributions of the HCO cofragment. HCO product state distributions have been derived following the population of various different N_{K_a} levels in the $\tilde{A}\,^1A_2$ $2^2 4^3$ and $2^3 4^1$ states. Two distinct spectral signatures are identified, suggesting competition between dissociation pathways involving the $\tilde{X}\,^1A_1$ and the $\tilde{a}\,^3A_2$ potential energy surfaces. Most rovibrational states of $H_2CO(\tilde{A}\,^1A_2)$ investigated in this work produce $H+HCO(\tilde{X}\,^2A')$ photofragments with a broad kinetic energy distribution and significant population in high energy rotational states of HCO. Photodissociation via the $\tilde{A}\,^1A_2$ $2^2 4^3$ $1_{1,1}$ (and $1_{1,0}$) rovibronic states yields predominantly HCO fragments with low internal energy, a signature that these rovibronic levels are perturbed by the $\tilde{a}\,^3A_2$ state. The results also suggest the need for further careful measurements of the H+HCO quantum yield from H_2CO photolysis at energies approaching, and above, the barrier to C–H bond fission on the $\tilde{a}\,^3A_2$ potential energy surface.
 [DOI: 10.1063/1.2752160]

INTRODUCTION

Despite several decades of intense study, formaldehyde and its derivatives continue to be the focus of much scientific research.[1–5] The basis of this interest lies in the many and diverse scientific subdisciplines to which formaldehyde chemistry applies. Spectral signatures of H_2CO have been observed in chemical environments ranging from combustion processes[6] to the interstellar medium[7] and have provided a means of monitoring atmospheric concentrations of the molecule.[8–13] Moreover, the photophysics of the perturbed excited rovibronic states of formaldehyde continues to elude a complete quantum chemical explanation. It is therefore not surprising that to spectroscopists the study of formaldehyde is particularly appealing.

A number of published computational studies[2,14–17] serve to complement the experimental investigations. The small size and discrete energy level structure of formaldehyde has permitted mapping of its potential energy surfaces (PESs) with the most accurate quantum chemistry methods and has facilitated studies of molecular processes such as nonradiative electronic transitions and photofragmentation.[18] It is hoped that the information garnered by following the progress of formaldehyde from its initial optically prepared state through to dissociation products via both experimental and *ab initio* methods will help to elucidate which parts of the molecular Hamiltonian control H_2CO photochemistry.

Photoinitiated unimolecular decomposition of formaldehyde by UV excitation yields two distinct product channels:

$$H_2CO \rightarrow H_2 + CO \tag{1}$$

$$\rightarrow H + HCO. \tag{2}$$

The threshold energies for product channels (1) and (2) are ~27 720 and 30 328.5 cm^{-1}, respectively.[19–21] Both of these processes are thought to occur via radiationless decay from the $\tilde{A}\,^1A_2$ state of formaldehyde, and both processes have been studied previously.[3,19,22–26] Here, we focus on the radical product channel.

A 1983 review by Clouthier and Ramsay discusses much of the historical spectroscopic information regarding formaldehyde,[27] though several articles have since refined this information.[1,28–31] Key to our discussion of the photochemical processes that generate the formyl radical are the $\tilde{X}\,^1A_1$, $\tilde{A}\,^1A_2$, and $\tilde{a}\,^3A_2$ electronic states of formaldehyde (also referred to as the S_0, S_1, and T_1 states, respectively, illustrated in Fig. 1) and the interactions between them. Although electronically forbidden, the $S_1 \leftarrow S_0$ transition shows

[a)]Authors to whom correspondence should be addressed.
[b)]Tel.: 1-613-533-2621; Fax: 1-613-533-6669. Electronic mail: hploock@chem.queensu.ca
[c)]Tel.: 44-117-9288312; Fax: 44-117-9250612. Electronic mail: mike.ashfold@bris.ac.uk

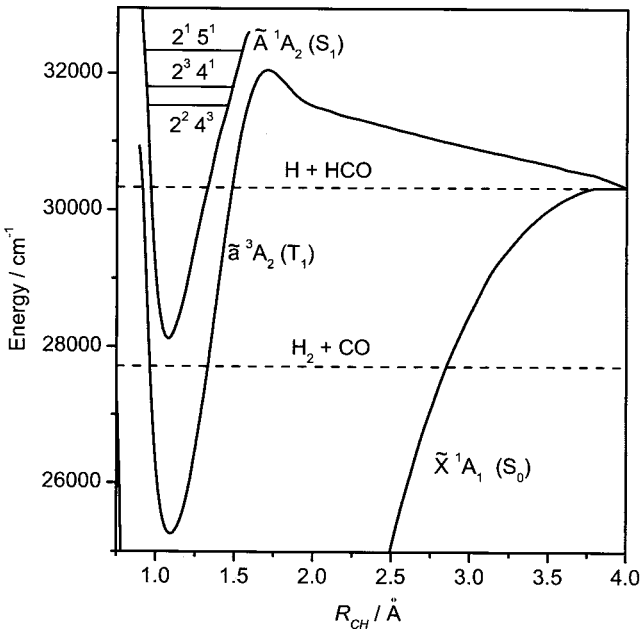

FIG. 1. Schematic potential energy surfaces for HCHO as a function of H–CHO bond distance. Both the S_0 and T_1 states correlate to the H+HCO radical products. Excitation to S_1 levels above the dissociation threshold can result in H+HCO formation either via internal conversion to high vibrational levels of S_0 or by intersystem crossing to the T_1 state. The dashed line at ~27 720 cm^{-1} indicates the onset energy for the formation of molecular products. Adapted from Ref. 21.

a weak vibronic origin band that is magnetic dipole allowed and exhibits progressions in ν_2' (C–O symmetric stretch) for the vibronically allowed 4_0^1 and 4_0^3 (C–H wag) transitions. Excitation to the S_1 state can result in fluorescence to low-lying S_0 vibronic states, internal conversion (IC) to high energy S_0 vibronic states, or intersystem crossing (ISC) to the T_1 PES.[3]

$S_1 \rightarrow S_0$ IC can yield both the H_2+CO and H+HCO products, provided minimum threshold energy requirements are met. $S_1 \rightarrow T_1$ ISC, on the other hand, produces H+HCO exclusively.[22] As a consequence, competition between the IC and ISC HCO formation mechanisms results, wherein dissociation occurs predominantly on the S_0 PES at threshold energies, whereas at energies near (and above) the T_1 barrier dissociation could occur on S_0 and/or T_1. This competition between dissociation mechanisms is influenced by several factors, which include (but are not limited to) (1) S_1-S_0 and S_1-T_1 coupling matrix elements, (2) T_1 barrier height, (3) proximities, densities, and widths of near-resonant T_1 energy levels and, below the T_1 barrier, (4) T_1 tunneling probabilities.[19]

The spectral region between 31 000 and 33 000 cm^{-1} is of particular interest since the minimum energy pathway over the T_1 barrier is predicted at ~32 350 cm^{-1}.[32] In this region, photodissociation channels can be accessed via the $S_1 \leftarrow S_0$ $2_0^2 4_0^3 (\bar{\nu}_0 = 31\,531.5\ \text{cm}^{-1})$, $2_0^3 4_0^1 (\bar{\nu}_0 = 31\,803.2\ \text{cm}^{-1})$, and $2_0^1 5_0^1 (\bar{\nu}_0 = 32\,334.6\ \text{cm}^{-1})$ vibronic bands. To the low wave number end of this region, S_1-T_1 coupling is expected to be small due to the low density (~0.3 T_1 states/cm^{-1}) and relatively narrow widths of near-resonant T_1 states.[19] With increasing energy, however, T_1 quantum state widths are expected to increase due to lifetime broadening as a result of quantum tunneling until, at energies above the T_1 barrier, S_1-T_1 coupling occurs via the T_1 dissociation continuum. In comparison, Stark level-crossing experiments have shown that S_0 quantum state widths are broad in this spectral region and that the density of S_0 states is expected to be significantly higher.[33] Nevertheless, S_1-S_0 coupling matrix elements are expected to be much smaller than those describing S_1-T_1 coupling.[19,33] For this reason, the formyl radical product pathway should evolve from an S_0 dominated dissociation mechanism at energies far below the T_1 barrier to a T_1 dominated mechanism at energies above this barrier.

In terms of product state distributions, the S_0 and T_1 dissociation pathways may be expected to yield very different photofragment internal energies. Internal conversion on the S_0 pathway leads to randomization of parent internal energies prior to dissociation, thereby favoring "statistical" quantum state population distributions in the photofragment products. That said, Suits and co-workers[23–26] have recently demonstrated that the CO fragments are formed with a bimodal rotational state population distribution, with a high J component attributable to a "roaming" H atom channel—essentially an intramolecular hydrogen abstraction following an (energetically frustrated) attempt at C–H bond fission on the S_0 PES. In contrast, H+HCO products formed as a result of coupling to the quasibound T_1 PES are expected to have high kinetic energies and only low levels of vibrational and rotational excitation.[19,22] Measurement of, and observations of variations in, product state distributions ought thus to offer insights into photodissociation mechanisms in the region of the T_1 barrier. In this study, we examine HCO product state distributions arising as a result of C–H bond fission following the population of specific rovibrational levels in the $\tilde{A}\ ^1A_2$ state of formaldehyde.

EXPERIMENT

The H atom (Rydberg) atom photofragment translational spectroscopy (PTS) studies were performed using a modified version of the experimental apparatus that has been described previously.[34,35] The experiments required that three laser beams, which have been detailed previously, be spatially overlapped in the center of the interaction volume, where they intercept a skimmed, pulsed, molecular beam of formaldehyde, seeded in argon. Nascent H atoms produced by the photolysis laser pulse are excited in a two-photon, double resonant excitation scheme to a Rydberg state with a high principal quantum number ($n \sim 80$). H atoms are first excited with Lyman-α radiation (121.6 nm generated by frequency tripling 364.7 nm radiation in phase matched Kr and Ar) from their $n=1$, $1s$ state to the $n=2$, $2p$ level. A second photon (365 nm) then further excites the electron to a high-n Rydberg state. "Rydberg tagged" H atoms with recoil velocities along the TOF axis travel under collision-free conditions to the detector (Johnston multiplier, type MM1-SG), where they are field ionized and their time of arrival recorded. Unwanted H^+ ions formed by 121.6 nm plus 364.7 nm absorption are extracted by applying a potential difference (50 V cm^{-1}) between a pair of annular electrodes positioned normal to the time of flight (TOF) axis above and below the

interaction volume. The H (Rydberg) TOF resolution was improved in this study by placing a 30×5 mm^2 slit shaped mask over the detector aligned with its long axis perpendicular to the molecular beam propagation axis. To detail the benefits of this mask, the resolution limits of the experiment are discussed in the Appendix.

Paraformaldehyde (prilled) was obtained commercially (Aldrich, 95%) and packed into a 7 μm stainless steel inline filter (Swagelok). Dried $MgSO_4$ was placed in a second filter further downstream, and both chemicals were kept in place with glass wool plugs. The filters were arranged behind the pulsed nozzle (in the order H_2CO, $MgSO_4$, and nozzle), and this entire arrangement was heated resistively to ~70 °C. The temperature was monitored with two thermocouples, positioned on the source oven and at the front of the nozzle. The paraformaldehyde liberates monomeric formaldehyde and water on heating. The $MgSO_4$ acts as a desiccant to absorb this water and stop the nozzle from clogging. Ar (~2 bars) was passed through the filters and the pulsed valve to form a pulsed supersonic expansion of H_2CO. The composition of the molecular beam was investigated by introducing a small TOF mass spectrometer within the apparatus, so that the interaction volume is positioned centrally within the first acceleration region, and using the 121.6 nm radiation as a photoionization source (for any species with ionization potential $E_i \leqslant 10.2$ eV). In order to confirm the presence of H_2CO in the beam and to probe the beam temperature, action spectra for forming H^+ ions via the fragmentation channel yielding H+HCO radicals were recorded. In the absence of the photolysis laser beam there was negligible ion signal. When the photolysis laser was introduced to the experiment, the H atoms formed by the photolysis of H_2CO were ionized by 121.6 nm radiation (and, by necessity, its 364.7 nm precursor). H^+ action spectra were then obtained by gating on the time of flight mass spectrometer H^+ output signal while scanning the photolysis laser so as to measure the wavelength dependence of H^+ ion production.

RESULTS AND DISCUSSION

The dissociation energy for the hydrogen atom and formyl radical product channel, $D_0(H-CHO)$, $=30\,328.5\pm0.5$ cm^{-1},[20] and the most accurate *ab initio* calculations to date place the maximum of the T_1 barrier (transition state) to dissociation between 1710 and 2130 cm^{-1} above the radical product asymptote.[32] The PESs in this region are shown in Fig. 1, and the $H_2CO(\tilde{A}\leftarrow\tilde{X})$ bands in this region are highlighted in the room temperature absorption spectrum shown in Fig. 2. The strongest features in the near threshold region for the H+HCO formation are the $\tilde{A}\,^1A_2 \leftarrow \tilde{X}\,^1A_1$ $2_0^1 4_0^3$, $2_0^2 4_0^1$, $2_0^2 4_0^3$, and $2_0^3 4_0^1$ vibronic bands, while the $2_0^1 5_0^1$ (overlapped with $1_0^1 2_0^1 4_0^1$) vibronic band spans the predicted energy of the exit channel barrier on the T_1 PES. Of particular interest in our attempt to probe the competition between the IC and ISC mechanisms of HCO formation are the $2_0^1 5_0^1$, $2_0^3 4_0^1$, and $2_0^2 4_0^3$ band systems, as these transitions represent excitation to energy levels at or slightly below the T_1 barrier.

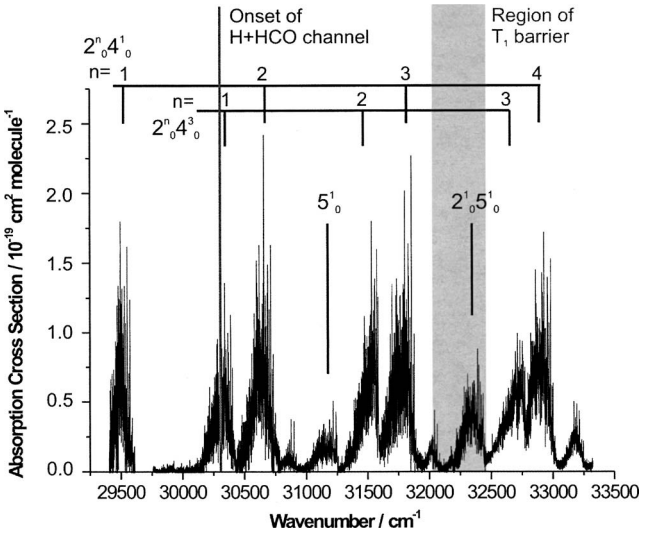

FIG. 2. Room temperature absorption spectrum of the relevant part of the HCHO ($\tilde{A}\,^1A_2\leftarrow\tilde{X}\,^1A_1$) band system. The most intense vibronic band features are labeled, as are the threshold energy for the onset of the radical product channel and the *ab initio* estimate for the T_1 transition state region. See Ref. 31 for details.

Both the T_1 and S_0 states correlate to radical products at infinite C–H bond distances. The S_1 PES couples to high vibrational levels of the electronic ground state (also referred to as S_0^* levels) via vibronic perturbations provided by the nuclear kinetic energy operator $\hat{T}_N$.[18,28] The magnitudes of the S_1-S_0^* matrix elements are expected to be less than 10^{-4} cm^{-1}.[22,33] However, the relatively high density of S_0^* states in the 31 000 and 33 000 cm^{-1} region [~100/cm^{-1} (Ref. 22)] facilitates an effective coupling between the S_1 and S_0 PESs. In comparison, $\tilde{A}\,^1A_2$ and $\tilde{a}\,^3A_2$ coupling matrix elements are much larger (0.01–0.1 cm^{-1}),[27] but their state mixing probability is offset by the relatively low density of T_1 states in the region [~0.3/cm^{-1} (Ref. 22)]. Moreover, because the T_1 PES is quasibound in the H+HCO near-threshold region, T_1 resonances are relatively sharp, leading to very localized regions of S_1-T_1 overlap. Coupling between the S_1 and T_1 PES is expected to increase with energy since T_1 resonances are increasingly broadened by quantum tunneling effects, until at energies above the T_1 transition state the triplet dissociation pathway is directly accessed via the T_1 dissociative continuum. Probing the dissociation characteristics in the near- and above-barrier regions should therefore provide a means of examining the dynamic signature for dissociation on the T_1 PES.

To determine which formaldehyde rovibronic levels could be populated and subsequently studied in our experiments, H^+ action spectra were recorded as a function of photolysis wave number (see Fig. 3). The various vibronic bands within this region of the H_2CO absorption spectrum were simulated with PGOPHER using refined constants from a recent study of accurate absorption cross sections for H_2CO.[31,36] A comparison of the simulated absorption spectrum with the experimental wavelength dependent yield of H^+ ions served to confirm the assignments of the observed rovibronic transitions and allowed the estimation of molecular beam temperatures. Sample spectral simulations are

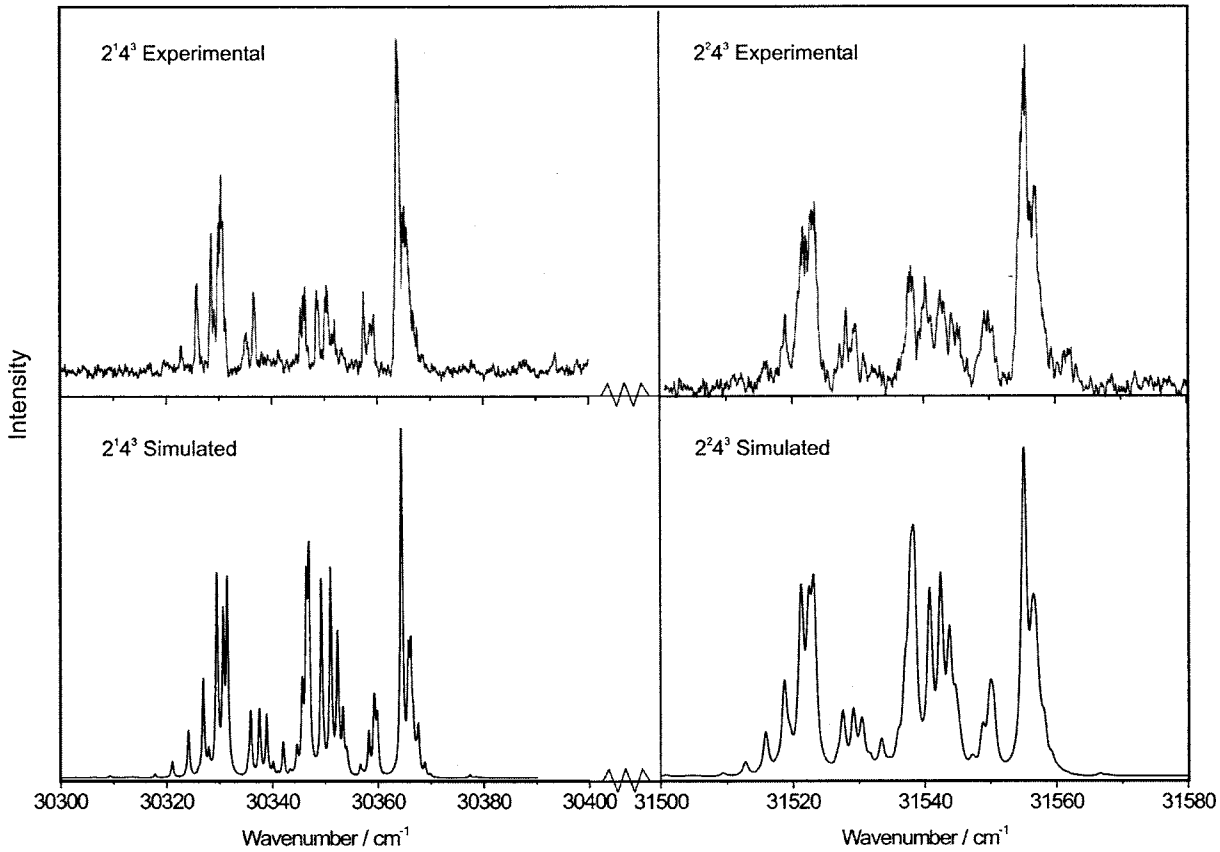

FIG. 3. H^+ action spectra as recorded following the photodissociation of formaldehyde in the $2_0^1 4_0^3$ and $2_0^3 4_0^1$ bands (top trace) and simulated absorption spectra for these bands (below). The simulations used PGOPHER (Ref. 36), spectroscopic constants as listed in Ref. 30, and assumed a rotational temperature of 10 K, and a transition lineshape determined by convoluting 0.1 cm^{-1} (FWHM) Gaussian width with a 0.45 cm^{-1} Lorentzian profile for lifetime effects.

shown in Fig. 3 along with the corresponding H^+ action spectra acquired during the excitation of the $\tilde{A}\,^1A_2 \leftarrow \tilde{X}\,^1A_1$ 2_0^1 and 4_0^3 bands. Immediately apparent is the H^+ signal at wave numbers $<30\,328$ cm^{-1}, which might appear to contradict the accepted value for D_0(H–CHO). These are, in fact, *P*-type excitations ($\Delta J=-1$) that terminate on energy levels above the lower limit for H-atom formation.

The spectral simulations shown in Fig. 3 allow determination of a rotational temperature T_{rot} of 10 K for the parent formaldehyde molecules though it should be pointed out that there are differences between the experimental and predicted line intensities that still elude definitive explanation. Possible reasons for these intensity discrepancies include (i) photodissociation of the primary HCO products and (ii) resonance enhanced two-photon excitation of H_2CO followed by dissociation, both of which will enhance the experimental H^+ signal at a given photolysis wavelength, and (iii) variations in S_1-level coupling efficiencies to S_0 and T_1 levels. Simulations of other vibronic bands produced T_{rot} values of up to 15 K, so we deduced that the actual rotational temperature of the formaldehyde parent molecules was ~10–15 K. Setting the photolysis laser to wavelengths corresponding to specific rovibronic transitions in formaldehyde enabled photodissociation from specific, known J_{K_a,K_c} levels in the $\tilde{A}\,^1A_2$ state. It is worth commenting here that, under these conditions, we were unable to detect any H atom signal at several wavelengths investigated in the earlier studies from Wittig's group. Only by reducing the argon backing pressure were we able to observe H atom signal at $\bar{\nu}=31\,768$ cm^{-1}, for example, which is one of the photolysis wave numbers for which data is reported in Ref. 19. PGOPHER simulations indicate that T_{rot} must be >50 K in order that the ground state level involved in this transition has an appreciable population.

H atom TOF spectra recorded after the dissociation of the C–H bond were analyzed in terms of the total kinetic energy release (TKER) for the system. The TKER can be defined in terms of the TOF, t_H, of the H atom,

$$\mathrm{TKER} = \tfrac{1}{2} m_H \left(1 + \frac{m_H}{m_R}\right)\left(\frac{d}{t_H}\right)^2, \tag{3}$$

where d is the distance between the laser interaction region and the detector, m_H and m_R are the masses of the H atom (1.0078 amu) and the HCO partner fragment (29.018 amu), respectively. The internal energy of the HCO fragment can then be established using conservation of energy arguments,

$$E_{phot} = D_0(\mathrm{H-CHO}) + E_{int} + \mathrm{TKER}, \tag{4}$$

where E_{phot} is the photon energy and E_{int} is the internal energy of the HCO fragment. The maximum kinetic energy release (minimum flight time) for the hydrogen atoms is available from

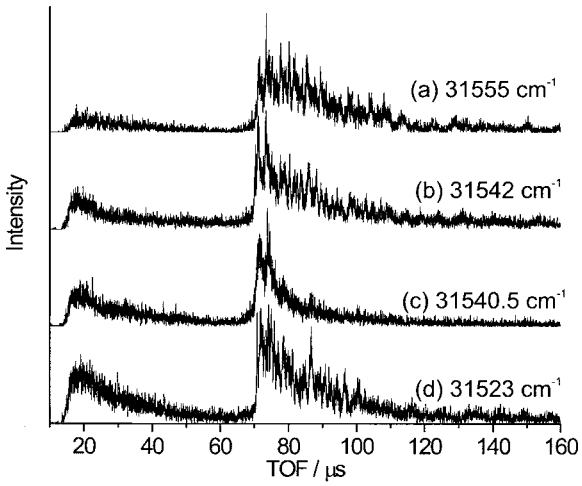

FIG. 4. TOF spectra of H atom photofragments resulting from the photolysis of jet-cooled formaldehyde molecules at (a) 31 555 cm^{-1}, (b) 31 542 cm^{-1}, (c) 31 540.5 cm^{-1}, and (d) 31 523 cm^{-1}. In each case the electric vector ε of the laser was aligned at 90° to the TOF axis.

$$\mathrm{TKER}_{\max} = E_{\mathrm{phot}} - D_0(\mathrm{H-CHO}), \tag{5}$$

(i.e., $E_{\mathrm{int}}=0$). For photodissociation to H+HCO from the $\tilde{A}\,^1A_2$ $2^2 4^3$ vibronic level at 31 555 cm^{-1}, the predicted $\mathrm{TKER}_{\max}$ is 1226.5 cm^{-1} (corresponding to $t_{\mathrm{H}}=70$ μs). This prediction is in very good agreement with the TOF spectra shown in Fig. 4. Worth noting further, however, are the yet faster hydrogen atom signals in the 14–60 μs range. Though inconsistent with one-photon dissociation to H+HCO products, a two-photon dissociation involving the same dissociative channel (i.e., giving an available energy $E_{\mathrm{avl}}=32\,780$ cm^{-1}) would produce hydrogen atoms with minimum $t_{\mathrm{H}}\sim 14$ μs, in very good accord with the experimental observation. Further support for this interpretation stems from the fact that the near H+HCO threshold bands of H_2CO show fluorescent lifetimes of 6–10 ns,[37] thereby indicating that the associated one-photon excited energy levels are potentially metastable resonant intermediates.

A closer inspection of the TKER spectral region corresponding to one-photon dissociation reveals a great deal of structure. This arises because the quantized nature of the formyl radical cofragment internal energies constrains the correlated hydrogen atom kinetic energies to values reflecting the HCO rovibrational structure throughout the available energy space. H atom TOF spectra may be replotted in terms of formyl radical internal energies according to Eq. (4). Using the HCO molecular parameters determined in the pure rotational microwave study by Blake *et al.*,[38] a term energy stick spectrum was generated, which facilitated the assignment of the HCO internal energy spectrum. The stick spectrum was then given a ~2 cm^{-1} linewidth (Gaussian, full width at half maximum) and was converted to a TKER spectrum for direct comparison with H atom TOFs. Line intensities were then adjusted to match approximately those of the

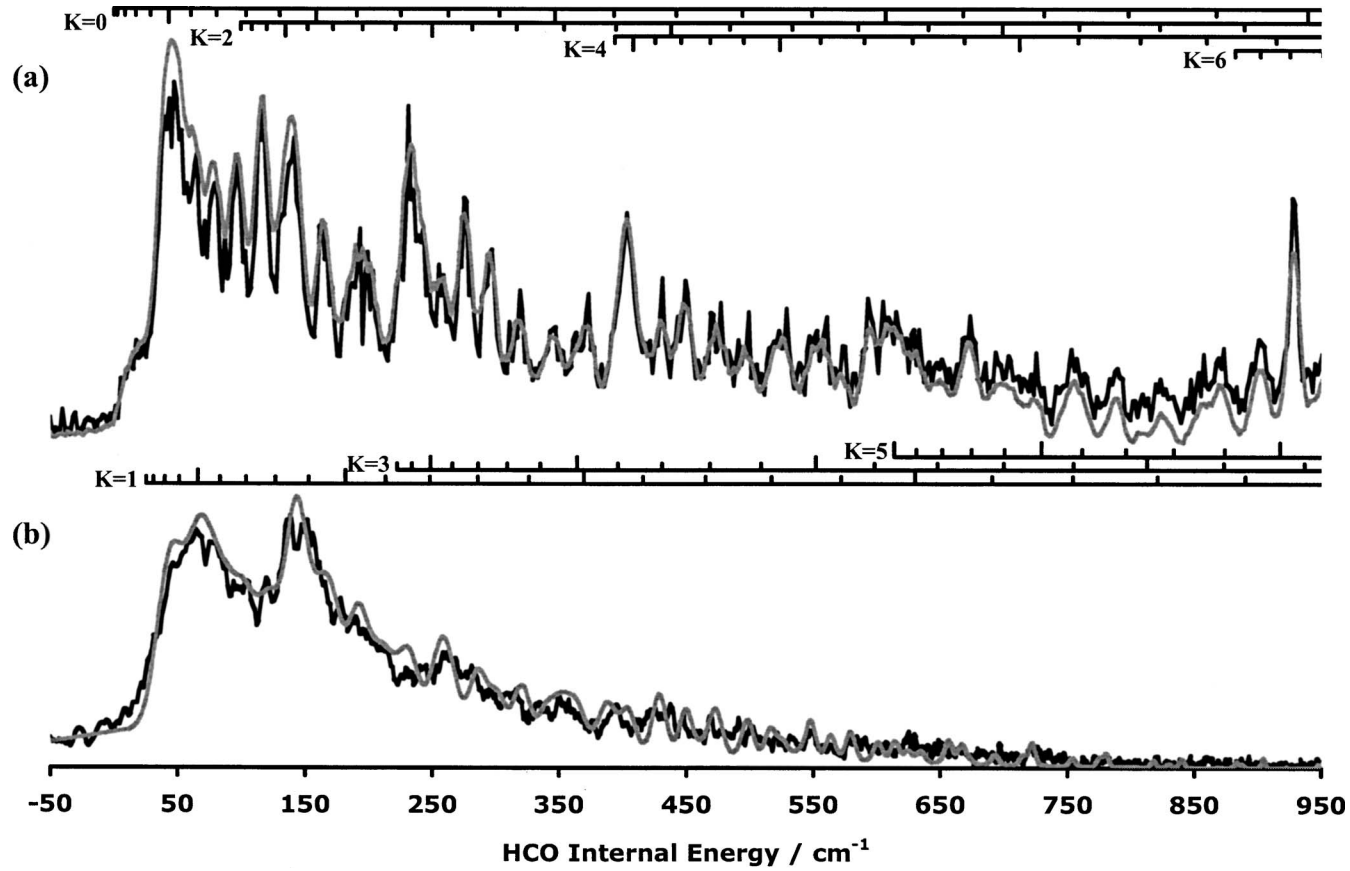

FIG. 5. Formyl radical internal energy spectra for H_2CO photolysis at (a) 31 522.1 cm^{-1} and (b) 31 540.5 cm^{-1}. The black traces are experimental spectra extracted from the H atom TOF data, while the gray traces are the fitted spectra used to extract product state distributions. Assignment combs are given to show HCO rotational energy levels with longer teeth marking N levels that are multiples of five.

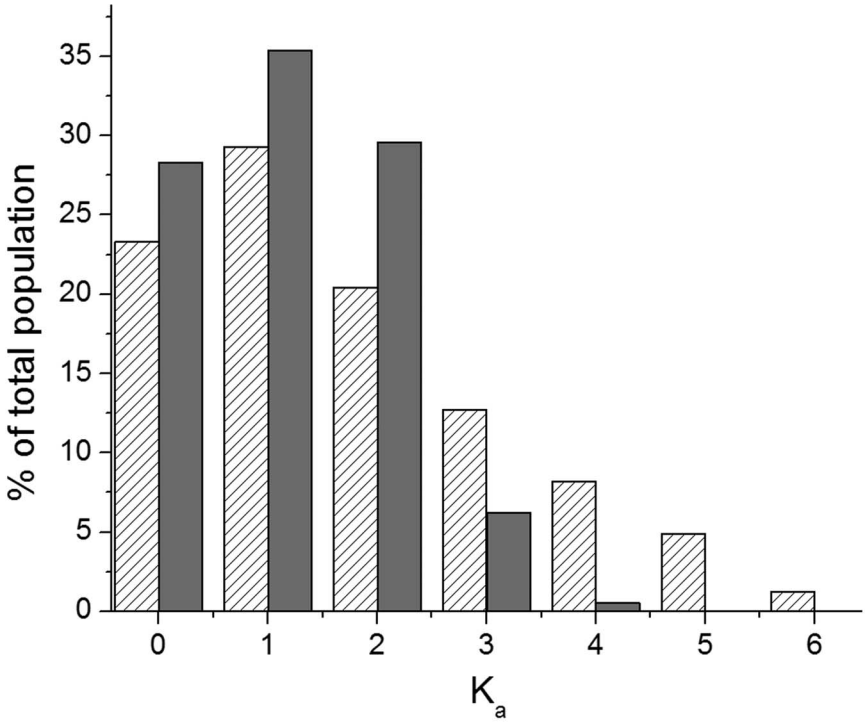

FIG. 6. Illustration of the variation in the K_a population distributions in the HCO($v=0$) fragments formed from H_2CO photolysis at 31 522.1 cm^{-1} (hatched) and 31 540.5 cm^{-1} (solid).

experimental spectrum using a Gaussian distribution for the K stacks, and a second Gaussian distribution for the N-level intensities within each K stack. To fit the simulated spectrum to the experimental data a gradient descent method was used to minimize least squares errors as a function of mean K standard deviation in K, mean N, standard deviation in N, spectral linewidth, and a small term to account for spectral term energy offset. The integrated spectral intensity was then normalized such that product state distributions could be extracted for each rotational level. Since there was no physical reason to assume that the spectral line intensity distributions should be described by Gaussian analytical functions of N and K_a, each of the line intensities in the predicted spectrum was then adjusted manually to reduce the fit residuals further. Each manual fit was repeated a total of three times as a means of estimating reproducibility. Comparisons of the experimental spectra and corresponding fitted spectra for H_2CO photolysis at 31 522.1 and 31 540.5 cm^{-1} are given in Figs. 5(a) and 5(b), respectively. The integrated K-stack product state distributions so derived are given in Fig. 6. Product state distributions derived for each HCO rotational energy level populated for the excitation wave numbers probed in our study are available as a supplementary material in the journal database.[39]

For the most part, the formyl radical cofragment formed during formaldehyde photolysis was found to have a population in rotational states extending throughout the available energy space. There were, however, notable exceptions to this that seem to be directly related to dissociation from specific rovibronic levels in the $\tilde{A}\ ^1A_2$ state. Figure 5(b), which shows the internal energy spectrum of HCO following the photolysis of H_2CO at 31 540.5 cm^{-1}, is one example. This excitation wave number corresponds to an $S_1 \leftarrow S_0\ ^rR$-type transition to the $\tilde{A}\ ^1A_2\ 2^2 4^3\ 1_{1,1}$ rovibronic level. As Fig. 6 shows, this dissociation yields HCO products with an integrated K state population distribution that is markedly different from the "more typical" distributions observed following excitation to other $\tilde{A}\ ^1A_2\ 2^2 4^3$ rovibronic levels (such as the $2_{0,2}$ level [Fig. 5(a)]). The concentration of population in low internal energy states following dissociation from the $\tilde{A}\ ^1A_2\ 2^2 4^3\ 1_{1,1}$ level is consistent with the mechanism for dissociation on the T_1 surface proposed by Wittig and co-workers,[19,22] suggesting that the $\tilde{A}\ ^1A_2\ 2^2 4^3\ 1_{1,1}$ level is directly perturbed by the $\tilde{a}\ ^3A_2$ state. This situation may also be described by estimating the fraction of E_{avl} partitioned into the product internal energy (E_{int}). An analysis of TKER spectra obtained following excitation within the $\tilde{A} \leftarrow \tilde{X}\ 2_0^2 4_0^3$ band at wave numbers other than 31 540.5 cm^{-1} gives an average value of $E_{int}/E_{avl}=0.29(7)\pm0.03(1)$, whereas dissociation via the $2^2 4^3\ 1_{1,1}$ level gives $E_{int}/E_{avl}=0.19(4)$. The errors given in brackets for the E_{int}/E_{avl} ratios are one standard deviation as determined by our fitting routine. Such analyses necessarily underestimate the E_{int}/E_{avl} ratio since the present experimental setup precludes detection of H atoms with near zero recoil velocities. Similar cold rotational distributions were found when dissociating via the $\tilde{A}\ ^1A_2\ 2^3 4^1\ 1_{1,1}$ and $1_{1,0}$ levels. Unfortunately, further confirmation of the dissociation signatures from these levels could not be made via other transitions due to lack of transition intensities or blending with other spectral lines.

In general, only levels characterized by the same quantum number J and the same overall symmetry species can perturb one another.[40] Given that there is no direct spin-orbit interaction between the $\tilde{A}\ ^1A_2$ and $\tilde{a}\ ^3A_2$ states, Stevens and Brand have discussed two mechanisms by which perturba-

tions can occur.[41,42] The selection rules for such perturbations can be summarized in terms of vibronic symmetries and rotational quantum numbers:

(i) vibronic spin-orbit mechanism

(a) $^1\Gamma_{ev} \times {}^3\Gamma_{ev} \supset R_a$; $\Delta J=0$, $\Delta N=0,\pm1$, $\Delta K_a=0$, $\Delta K_c=\pm1$,

(b) $^1\Gamma_{ev} \times {}^3\Gamma_{ev} \supset R_b$; $\Delta J=0$, $\Delta N=0,\pm1$, $\Delta K_a=\pm1$, $\Delta K_c=\mp1,\mp3$

(c) $^1\Gamma_{ev} \times {}^3\Gamma_{ev} \supset R_c$; $\Delta J=0$, $\Delta N=0,\pm1$, $\Delta K_a=\pm1$, $\Delta K_c=0,\mp2$

(ii) spin-orbit orbital-rotation mechanism

(a) $^1\Gamma_e={}^3\Gamma_e$, $^1\Gamma_{ev}={}^3\Gamma_{ev}$, $\Delta J=0$, $\Delta N=0,\pm1$, $\Delta K_a=0,\pm2$, $\Delta K_c=0,\mp2$.

Since the ν_2 and ν_4 normal modes of the $\tilde{A}\,^1A_2$ state have a_1 and b_1 symmetries, the overall vibronic symmetry species for the 2^24^3 and 2^34^1 levels is B_2 in both cases. In the absence of rotation, the three components of the triplet state have A_1, B_1, and B_2 spin-orbital symmetries. The rotational symmetries about the a, b, and c axes are a_2, b_1, and b_2, respectively. For the $\tilde{a}\,^3A_2$ state to perturb the $\tilde{A}\,^1A_2$ 2^24^3 and 2^34^1 levels, triplet state vibronic species of B_1, A_2, or A_1 symmetry must undergo a-, b-, or c-type Coriolis interactions. The A_1 spin component must therefore have a b_1, a_2, or a_1 vibrational symmetry, the B_1 spin component must have an a_1, b_2, or b_1 vibrational symmetry, and the B_2 spin component must have an a_2, b_1, or b_2 vibrational symmetry to facilitate interaction with the $\tilde{A}\,^1A_2$ state via the above-mentioned Coriolis mechanisms. This implies that $\tilde{a}\,^3A_2$ vibrational levels of any symmetry can potentially perturb the $\tilde{A}\,^1A_2$ 2^24^3 and 2^34^1 levels. To perturb the $\tilde{A}\,^1A_2$ 2^24^3 level the triplet state would require $\sim$6350 cm^{-1} of vibrational excitation, while $\sim$6620 cm^{-1} of vibrational excitation is needed to achieve close resonance with the $\tilde{A}\,^1A_2$ 2^34^1 vibronic level. Several T_1 vibrational levels fall in this energy region, but until there is a better knowledge of the fundamental vibrational frequencies and anharmonicities for the $\tilde{a}\,^3A_2$ state the perturbing T_1 vibrational levels cannot be assigned unambiguously. What is clear, however, is that observation of such localized variations in the N, K level population distributions in the HCO products must imply rather stringent resonance requirements on these S_1-T_1 perturbations, i.e., that the T_1 resonance widths at these energies (below the top of the T_1 barrier) are narrow.

Several singlet-triplet perturbations in the 2^24^3 and 2^34^1 levels of formaldehyde have been previously observed by Ramsay and Till using magnetic rotation spectroscopy.[43] However, their spectra were taken in a room temperature cell with a 10 Torr pressure of formaldehyde, and none of the excitations observed in our study were reported. Similar studies of the 4_0^1 and 4_0^3 bands by Kerr *et al.* also identified singlet-triplet perturbations in the $\tilde{A}\,^1A_2$ 4^1 and $\tilde{A}\,^1A_2$ 4^3 levels.[44] A series of magnetically active lines involving $J'=16-19$ in several K_a levels of the 4_0^3 band suggests a singlet-triplet perturbation with selection rules $\Delta J=0$, $\Delta N=0$, and $\Delta K_a=0$ since near-resonant interactions governed by these selection rules could involve several successive values of K_a, whereas a $\Delta K_a=\pm1$ perturbation would likely affect only one or two K_a values. These perturbations were attributed to the F_2 spin component ($J=N$) of the $\tilde{a}\,^3A_2$ $4^15^16^1$ vibronic level. Given that the observed F_2 perturbations occurred at relatively high J values in the 4^3 level, it would stand to reason that the F_3 spin component ($J=N-1$) should cross the singlet manifold at low J levels and perturb those near-resonant rovibronic states following a $\Delta K_a=\pm1$ selection rule. Since the ν_2 harmonic vibrational frequencies for the $\tilde{A}\,^1A_2$ and the $\tilde{a}\,^3A_2$ states are similar,[27] it is tempting to attribute the unique product state distributions arising from the dissociation of the $\tilde{A}\,^1A_2$ 2^24^3 $1_{1,1}$ state to a perturbation involving the $2^24^15^16^1$ 1_0 $(J_{,K_a})$ level of the $\tilde{a}\,^3A_2$ F_3 spin component. Similar arguments can be made in an attempt to assign the triplet state that perturbs the $\tilde{A}\,^1A_2$ 2^34^1 $1_{1,0}$ level. However, the large number of magnetically active lines observed in the $2_0^24_0^3$ and $2_0^34_0^1$ bands belies the presence of at least two (likely more) perturbing triplet levels.

TABLE I. $N_{v3=1}/N_{v=0}$ vibrational state population ratios in the HCO fragments formed following dissociation from various rotational levels of the $\tilde{A}\,^1A_2$ 2^34^1 vibronic state of H_2CO.

Photolysis wave number (cm^{-1})	H_2CO $\tilde{A}\,^1A_2$ 2^34^1 rotational state(s)	$N_{v3=1}/N_{v=0}$
31 829.0	$2_{2,0}$ and $2_{2,1}$	0.29
31 814.5	$2_{1,2}$	0.25
31 812.8	$1_{1,1}$	0.20
31 810.5	$1_{1,0}$	0.10
31 798.0	$3_{1,3}$	0.17
31 794.4	$1_{0,1}$	0.21
31 793.5	$2_{0,2}$	0.22

When the H+HCO dissociation channel is accessed from the $\tilde{A}\,^1A_2$ 2^34^1 state, E_{av1} is sufficient that the first excited vibrational level ($v_3=1$) of HCO can be observed in the TKER spectra. Wittig and co-workers suggested that the $v_3=1:v=0$ population ratio provides another measure of the relative importance of dissociation via coupling to the S_0 and/or T_1 PESs,[19,22] and a careful analysis of the present, better resolved TKER spectra lends some support to this proposal. As Table I shows, the vibrational state population ratio $N_{v3=1}/N_{v=0}$ [crudely estimated from the relative amounts of the signal with E_{int}, respectively, above and below 1087 cm^{-1} (the $v_3=1$ term value), after background correction] is consistently low (in the range 0.10–0.29) but is lowest when exciting via the 2^34^1 $1_{1,0}$ level, which, by virtue of the deduced rotational state population distribution, we deem to be heavily perturbed by the T_1 state. We recognize three systematic errors in these estimations of vibrational population ratios. Firstly, as noted previously, the present experimental setup precludes measurement of products with zero TKER. The measured TOF data were truncated at an upper limit of 159 μs, thereby excluding photofragmentation processes yielding products with TKER <238 cm^{-1}. Secondly, the inverse square relationship between the measured H atom TOF and the product TKER can introduce an error in as much as any stray counts (that tend to appear randomly in

time) make a disproportionate contribution to the low TKER signal. To compensate for such effects, a linear background was subtracted as and when necessary from the measured TOF profiles prior to transformation to TKER. Obviously, any population ratios derived as above are sensitive to the extent of any such subtraction. Finally, HCO($v=0$) products formed in rotational states with high N, K quantum numbers have comparable energies to those of HCO($v_3=1$), low N products, and thus appear at comparable TKERs. As Fig. 6 shows, dissociation via the S_0 PES results in a broader rotational state population distribution. Our attribution of all signal with $E_{\text{int}} > 1089\ \text{cm}^{-1}$ to HCO($v_3=1$) products is thus likely to result in an overestimation of the $N_{v3=1}/N_{v=0}$ ratio in such cases and may explain, at least partly, the trends in this ratio displayed in Table I.

The observed vibrational excitation in the HCO products qualitatively supports the conclusions reached in an earlier study by Yin *et al.*[3]—specifically that HCO products formed from $\tilde{A}\ ^1A_2$ state levels that are perturbed by the $\tilde{a}\ ^3A_2$ state carry population in the 3^1 level, even when formed following excitation at energies above the T_1 transition state. In their study, Yin *et al.* employed laser-induced fluorescence (LIF), on the $\tilde{B}\ ^2A' \leftarrow \tilde{X}\ ^2A'$ transition, to probe the HCO fragments in their ground and 3^1 levels. Of necessity, these were probed via different vibronic transitions (the 0_0^0 and 3_1^0 bands). Although experimental considerations such as dye laser power curves were taken into account when relating the relative intensities of these bands, Yin *et al.*[3] had no rigorous means of accounting for differences in the Franck-Condon factors for the two transitions in their analysis. Bruna *et al.*[45] and Sappey and Crosley[46] both suggested that the Franck-Condon factors for the two probe transitions should be significantly different, with those for the 3_1^0 band as much as two to three times larger than that for the 0_0^0 band. We therefore provide complementary insight into vibrational branching ratios since, as discussed above, the intensity intensities of the H (Rydberg) TOF signals are largely unbiased against the vibrational state of the HCO cofragment.

As Fig. 7 shows, dissociation from the $\tilde{A}\ ^1A_2\ 2^15^1$ state of formaldehyde yields HCO radical fragments with both rotational and vibrational energy distributions more similar to those observed following dissociation via the $\tilde{A}\ ^1A_2\ 2^24^3\ 1_{1,1}$ and $\tilde{A}\ ^1A_2\ 2^34^1\ 1_{1,0}$ states. Such internal energy distributions are consistent with a dissociation mechanism directly accessing the T_1 surface. Given the energies of the rotational levels in question, S_1-T_1 coupling likely occurs via the T_1 dissociative continuum. A quantitative analysis to extract product state distributions could not be undertaken for this series of data, however, due to a much poorer signal to noise ratio, the origin of which is twofold. First, as is apparent in Fig. 2, the absorption cross section for the $\tilde{A}\ ^1A_2 \leftarrow \tilde{X}\ ^1A_1\ 2_0^15_0^1$ transition is less than that of the $2_0^24_0^3$ or $2_0^34_0^1$ vibronic bands, resulting in less excited state population and thus a reduced H atom PTS signal. Second, the increased fragment kinetic energies mean that the TOF spectra of interest now overlap with the tails of the two-photon dissociation signal. Nevertheless, qualitatively, it is clear that there is again some population (10%–30%) in the HCO 3^1 vibrational level when exciting via the $2_0^15_0^1$ transition. Thus, we concur with another conclusion reached by Yin *et al.*,[3] i.e. that the extent of the HCO product rotation provides the most robust signature of the fragmentation pathway. Dissociation via the S_0 PES results in the population of high N, K states of HCO, whereas S_1-T_1 coupling leads to HCO products with low internal excitation.

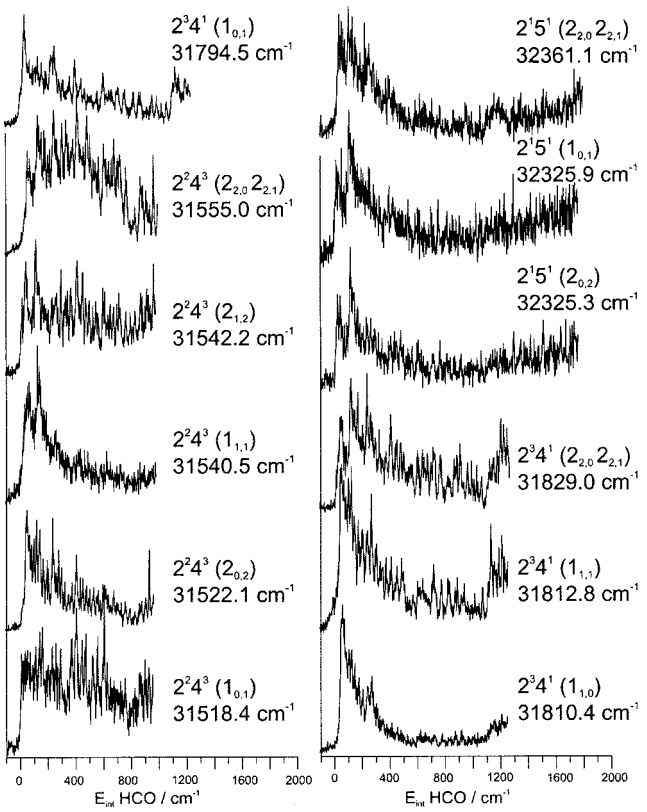

FIG. 7. H+HCO TKER spectra for formaldehyde photolysis plotted in terms of formyl radical internal energies. Photolysis wave numbers are given along with the $\tilde{A}\ ^1A_2$ rovibrational state(s) populated. In each case the electric vector ε of the laser radiation was aligned at 90° to the TOF axis.

Finally, it is worth considering the possible significance of the present findings with regard to the quantum yield, Φ_R, of the radical (i.e., H+HCO) channel following UV photolysis of formaldehyde and its dependence on wavelength λ. Both of these photofragments contribute to HO_x production in the upper troposphere.[47] The current NASA recommendation[48] shows Φ_R (298 K)>0 once $\lambda < 341$ nm, rising to a value of ~ 0.75 by $\lambda \sim 315$ nm and thereafter remaining flat down to $\lambda \sim 300$ nm. The maximum value of Φ_R (~ 0.75) stems from early end-product analysis measurements by Horowitz and Calvert;[49] subsequent determinations of Φ_R (Refs. 50–54) have generally involved relative measurements, which have been put on an absolute scale by normalizing to the early results. The current consensus[18,22] is that ISC is the dominant nonradiative decay process from S_1 levels lying at energies above the exit channel barrier on the T_1 PES and that its rate (relative to $S_1 \rightarrow S_0$ IC) should increase with increasing energy. Such is consistent with the present observation that the HCO products resulting from dissociation via the 2^15^1 level are internally cold and with the findings of an early PTS study (at 283.9 nm) which failed

to detect any CO attributable to the molecular (H_2+CO) product channel: signal to noise and resolution issues led to the (conservative) conclusion that $(1-\Phi_R) < 0.1$ at this wavelength.[55] We do note, however, that excitation at a narrow range of energies just above the T_1 barrier region (32 700–32 900 cm^{-1}) has been shown to yield H+HCO products with an E_{int} distribution more characteristic of a dissociation mechanism involving $S_1 \rightarrow S_0$ IC.[22] Since neither the S_1 nor T_1 states of H_2CO correlate directly with molecular products, IC from S_1 is the only straightforward route to forming H_2+CO. It is thus not easy to reconcile the consensus view that the fraction of S_1 molecules decaying via the IC route falls with increasing excitation energy (as the rate of $S_1 \rightarrow T_1$ ISC grows), with the recommendation that Φ_R is wavelength independent, yet nonlimiting, in the wavelength range $310 > \lambda > 290$ nm.[48] There remains a need for further careful studies of the branching into radical and molecular products [channels (1) and (2)] and their wavelength dependence.

CONCLUSIONS

The benefits of using a strategically masked detector in photofragment translational spectroscopic studies of H_2CO are demonstrated. The H atom TOF spectra display resolved structure, attributable to the population of rotational states of the formyl partner fragment. A spectral analysis has allowed extraction of HCO rotational state population distributions following H_2CO dissociation via selected rotational levels of the $\tilde{A}\ ^1A_2 2^2 4^3$ and $\tilde{A}\ ^1A_2 2^3 4^1$ vibronic states. Dissociation of $H_2CO(S_1)$ molecules to radical products involves radiationless transfer to the T_1 and/or S_0 PESs. Consistent with early H (Rydberg) PTS studies,[19,22] we find that HCO products arising via the $S_1 \rightarrow S_0$ IC route are characterized by broad rotational state population distributions, whereas those formed via dissociation on the T_1 PES (following $S_1 \rightarrow T_1$ ISC) are concentrated in low N, K states. These different product energy disposals have allowed the identification of specific parent S_1 levels, within both the $2^2 4^3$ and $2^3 4^1$ vibronic states, that appear to be perturbed by the T_1 state. Both fragmentation pathways lead to 10%–30% vibrational excitation of the HCO product, qualitatively supporting conclusions reached in a recent LIF study of the HCO products resulting from H_2CO photolysis in the same UV wavelength region.[3]

Recent studies by Tulej *et al.*[56] serve to emphasize the fact that we must be resigned to some variation in product state distributions derived in different H_2CO photodissociation studies. The parent absorption spectrum consists of many predissociation broadened lines; thus, the relative populations projected to the S_1 state in any photoexcitation process will depend not just on the precise excitation laser wavelength and bandwidth, but also on the parent rotational temperature since the latter will affect the relative weightings of the various components contributing to any blended absorption lines. Given that each (v', J', K_a') level of the S_1 parent yields its own specific H+HCO product state distribution (PSD), the observed PSD following any given photolysis event has to be viewed as a superposition of the PSDs characteristic to each of the dissociating levels, weighted by the respective Boltzmann populations, line strength factors, etc.

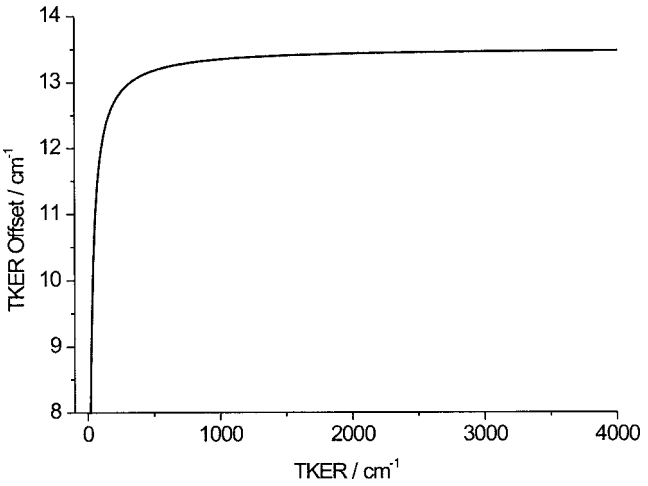

FIG. 8. Offset due to the c.m. to lab conversion shown as a function of TKER for the case of H+HCO fragments.

ACKNOWLEDGMENTS

After completion of this work we were alerted to further work from Yin *et al.* (Ref. 57). The authors would like to thank Professor Scott Kable, Professor Andrew Orr-Ewing, Dr. Pablo Bruna, Dr. Colin Western, Chris Clouthier, Nick Trefiak, and Maryam Moradi for helpful discussions and aid in data processing. Two of the authors (W.S.H. and H.-P.L.) would like to acknowledge funding from the Natural Sciences and Engineering Research Council of Canada (NSERC), and H.-P.L. acknowledges financial support through the Gordon and Jean Southam Fellowship of the Association of Commonwealth Universities. The Bristol authors are grateful to EPSRC for the award of the LASER portfolio grant.

APPENDIX: IMPROVEMENT OF THE TOF RESOLUTION

The H (Rydberg) TOF resolution was improved in this study by placing a 30×5 mm^2 slit shaped mask over the detector. The slit was aligned with its long axis (30 mm) perpendicular to the molecular beam propagation axis. To appreciate the benefits of this mask, the resolution limits of the experiment must be discussed. Some of these topics have been dealt with previously in theses from the Bristol research group.[58–60]

Experimentally recorded H atom TOF spectra are analyzed in terms of TKER for the system in question as outlined in Eq. (1). A small correction must be made to this derived TKER to account for the difference between the laboratory (lab) and center of mass (c.m.) frames of reference due to the velocity component of the molecular beam orthogonal to the TOF axis. For an expansion in Ar (v_{beam} ~ 557 m s^{-1}) the c.m. to lab correction factor is ~ 13 cm^{-1} and varies as shown in Fig. 8.

The TOF to TKER or velocity transformation assumes that all H atoms striking the detector travel a distance d from the interaction region. In reality, a detector of finite area is required to achieve sufficient signal to record TOF spectra with an acceptable signal to noise ratio. H atoms striking opposite edges of the detector have different flight distances. This implies that H atoms with slightly different kinetic energies can reach the detector at the same time. The distance traveled by an H atom that hits the edge of the detector, d_e is greater than that for a particle that strikes the center, d, thereby introducing an uncertainty to the TKER distribution and limiting the experimental resolution.

For the circular detector the flight distance from the interaction point to the detector edge is given in terms of the detector radius r by

$$d_e = \sqrt{d^2 + r^2}. \tag{A1}$$

The uncertainty in the TKER for a given flight time then becomes

$$\Delta\mathrm{TKER} = \frac{1}{2} m_{\mathrm{H}} \left(1 + \frac{m_{\mathrm{H}}}{m_{\mathrm{R}}}\right) \frac{d^2}{t^2} \left(\frac{r^2}{d^2}\right) = \mathrm{TKER}\left(\frac{r^2}{d^2}\right). \tag{A2}$$

For a 15 mm radius detector and a flight length of 371 mm the uncertainty in the TKER resolution limit is 1.6 cm^{-1} for a TKER of 1000 cm^{-1}. In the case of HCHO, where the initial excitation is rovibronically state selective, the peak widths of the internal energy states of HCO are $\sim$2–3 cm^{-1}. One must also account for the relative orientation of the detector to the expanding Newton sphere. In the lab frame the face of the detector lies perpendicularly to the TOF axis, but in the c.m. frame the contribution of the velocity of the molecular beam causes the H atoms to approach the detector obliquely. This is particularly significant for slow H atoms and results in an increased uncertainty in the flight distance. The uncertainty is largest for H atoms traveling with velocities comparable to the molecular beam speed but can be the limiting factor in resolution even with relatively fast H atoms. Note that this effect is only relevant in the molecular beam propagation axis as the beam has a negligible velocity component in all other coordinates.

The angle α between the molecular beam axis and the TOF axis in the c.m. frame is

$$\alpha = \tan^{-1}\left(\frac{v_{\mathrm{lab}}}{v_{\mathrm{beam}}}\right). \tag{A3}$$

The offset x of the c.m. along the molecular beam axis is defined in terms of the flight distance to the center of the detector as

$$x = \frac{d}{\tan\alpha} = \frac{d v_{\mathrm{beam}}}{v_{\mathrm{lab}}}. \tag{A4}$$

The effective flight lengths to the center ($d_{\mathrm{c.m.}}$) and the edges of the detector [$d^{\mathrm{F}}_{\mathrm{c.m.}}$ (far), $d^{\mathrm{N}}_{\mathrm{c.m.}}$ (near)] in the c.m. frame depend on this offset, which in turn depends on the relative H atom lab frame and molecular beam velocities (see Fig. 9),

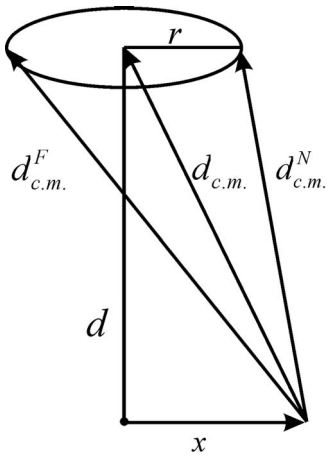

FIG. 9. Illustration showing the relationship between the flight distances d in the c.m. frame to the center of the detector and the near N and far F edges of the detector.

$$d_{\mathrm{c.m.}} = \sqrt{x^2 + d^2}, \tag{A5}$$

$$d^F_{\mathrm{c.m.}} = \sqrt{(x + r)^2 + d^2}, \tag{A6}$$

$$d^N_{\mathrm{c.m.}} = \sqrt{(x - r)^2 + d^2}. \tag{A7}$$

The uncertainty in flight length is a significant contribution to the resolution limit at all kinetic energies. With an increasing H atom velocity, the offset in the c.m. frame tends to zero and the geometry approaches the lab geometry. Under these circumstances the resolution limit approaches that imposed by the fixed cone angle (described above in Eq. (A2)) and is determined by the relationship between the flight length and the radius of the detector. For noninfinite velocities, the offset between the c.m. and lab frames is the limiting factor for instrumental resolution. Other possible resolution limiting factors include a spread of internal energies in the parent molecules (should be minimized in the molecular beam), the finite size of the interaction volume which is defined by the laser beam overlap region, and any spread in the molecular beam velocity.

One approach to alleviate the resolution limit imposed by the lab/c.m. offset involves decreasing the cone angle and therefore the uncertainty in the flight length. This can be done either by increasing the length of the TOF tube or by using a detector with a smaller radius. As the H atom flux decreases quadratically with the diameter of the detector, this approach is only possible in systems that yield a large number of H atoms per laser shot. The major contribution to the uncertainty is the orientation of the detector relative to the c.m. The c.m. frame is dependent on the molecular beam, and the molecular beam only has a velocity component in one direction. Therefore, it is only necessary to limit the size of the detector in the direction of the molecular beam axis. A mask with a slit shaped geometry minimizes the detector size in the direction of the molecular beam but gives the maximum open area. This geometry therefore minimizes the uncertainty in the flight length while maintaining a workable H atom flux. The resolution achieved here is unsurpassed by alternative systems, but the signal was reduced significantly

with the mask. The technique is, therefore, not appropriate for systems with absorption cross sections much smaller than that of formaldehyde nor is it necessary for systems where rotational resolution is not achievable due to a higher density of states. Regardless of the shape of the detector, slow H atoms are underdetected in this system. Simple correction factors, based on geometry, can be applied to the data to alleviate this minor complication.

[1] R. Perez, J. M. Brown, Y. Utkin, J. Han, and R. F. Curl, J. Mol. Spectrosc. **236**, 151 (2006).
[2] D. P. Chong and Y. Takahata, Chem. Phys. Lett. **418**, 286 (2006).
[3] H. M. Yin, S. H. Kable, X. Zhang, and J. M. Bowman, Science **311**, 1443 (2006).
[4] J. C. Weisshaar and C. B. Moore, J. Chem. Phys. **70**, 5135 (1979).
[5] T. W. R. Hancock and R. N. Dixon, J. Chem. Soc., Faraday Trans. **93**, 2707 (1997).
[6] C. Brackmann, J. Nygren, X. Bai, Z. Li, H. Bladh, B. Axelsson, I. Denbratt, L. Koopmans, P.-E. Bengtsson, and M. Alden, Spectrochim. Acta, Part A **59**, 3347 (2003).
[7] K. M. Menten and M. J. Reid, Astrophys. J. **465**, L99 (1996).
[8] C. Hak, I. Pundt, S. Trick *et al.*, Atmos. Chem. Phys. **5**, 2881 (2005).
[9] A. Heckel, A. Richter, T. Tarsu, F. Wittock, C. Hak, I. Pundt, W. Junkermann, and J. P. Burrows, Atmos. Chem. Phys. **5**, 909 (2005).
[10] M. Grutter, E. Flores, G. Andraca-Agala, and A. Baez, Atmos. Environ. **39**, 1027 (2005).
[11] C. Roller, A. Fried, J. Walega, P. Weibring, and F. Tittel, Appl. Phys. B: Lasers Opt. **82**, 247 (2006).
[12] Y. Q. Li, K. L. Demerjian, M. S. Zahniser, D. D. Nelson, J. B. McManus, and J. C. Herndon, J. Geophys. Res. **109**, D16S08 (2004).
[13] S. R. Utembe, M. E. Jenkin, R. G. Derwent, A. C. Lewis, J. R. Hopkins, and J. F. Hamilton, Faraday Discuss. **130**, 311 (2005).
[14] M. Peric, F. Grein, and M. R. J. Hachey, J. Chem. Phys. **113**, 9011 (2000).
[15] M. R. J. Hachey and F. Grein, Chem. Phys. Lett. **256**, 179 (1996).
[16] M. R. J. Hachey, P. J. Bruna, and F. Grein, J. Chem. Soc., Faraday Trans. **90**, 683 (1994).
[17] V. Galasso, J. Chem. Phys. **92**, 2495 (1990).
[18] J. C. Weisshaar and C. B. Moore, Annu. Rev. Phys. Chem. **34**, 525 (1983).
[19] M. J. Dulligan, M. F. Tuchler, J. Zhang, A. Kolessov, and C. Wittig, Chem. Phys. Lett. **276**, 84 (1997).
[20] A. C. Terentis and S. H. Kable, Chem. Phys. Lett. **258**, 626 (1996).
[21] A. C. Terentis, S. E. Waugh, G. F. Metha, and S. H. Kable, J. Chem. Phys. **108**, 3187 (1998).
[22] L. R. Valachovic, M. F. Tuchler, M. J. Dulligan, Th. Droz-Georget, M. Zyrianov, A. Kolessov, H. Reisler, and C. Wittig, J. Chem. Phys. **112**, 2752 (2000).
[23] D. Townsend, S. A. Lahankar, S. K. Lee, S. D. Chambreau, A. G. Suits, X. Zhang, J. Rheinecker, L. G. Harding, and J. M. Bowman, Science **306**, 1158 (2004).
[24] S. D. Chambreau, S. A. Lahankar, and A. G. Suits, J. Chem. Phys. **125**, 044302 (2006).
[25] S. A. Lahankar, S. D. Chambreau, D. Townsend, F. Suits, J. Farnum, J. M. Bowman, X. Zhang, and A. G. Suits, J. Chem. Phys. **125**, 044303 (2006).
[26] S. A. Lahankar, S. D. Chambreau, X. B.Zhang, J. M. Bowman, and A. G. Suits, J. Chem. Phys. **126**, 044314 (2007).
[27] D. J. Clouthier and D. A. Ramsay, Annu. Rev. Phys. Chem. **34**, 31 (1983).
[28] W. H. Green, Jr., C. B. Moore, and W. F. Polik, Annu. Rev. Phys. Chem. **43**, 591 (1992).
[29] S. Brunken, H. S. P. Muller, F. Lewen, and G. Winnewisser, Phys. Chem. Chem. Phys. **5**, 1515 (2003).
[30] X. Bai, T. Metz, F. Ossler, and M. Alden, Spectrochim. Acta, Part A **60**, 821 (2004).
[31] C. A. Smith, F. D. Pope, B. Cronin, C. B. Parkes, and A. J. Orr-Ewing, J. Phys. Chem. A **110**, 11645 (2006).
[32] Y. Yamaguchi, S. S. Wesolowski, T. J. Van Huis, and H. F. Schaefer III, J. Chem. Phys. **108**, 5281 (1998).
[33] W. F. Polik, D. R. Guyer, and C. B. Moore, J. Chem. Phys. **92**, 3453 (1990).
[34] L. Schneider, W. Meier, K. H. Welge, M. N. R. Ashfold, and C. M. Western, J. Chem. Phys. **92**, 7027 (1990).
[35] B. Cronin, M. G. D. Nix, A. L. Devine, R. N. Dixon, and M. N. R. Ashfold, Phys. Chem. Chem. Phys. **5**, 599 (2006).
[36] C. M. Western, PGOPHER, a program for simulating rotational structure, University of Bristol, 2005 (http://pgopher.chm.bris.ac.uk).
[37] H. L. Selzle and E. W. Schlag, Chem. Phys. **43**, 111 (1979).
[38] G. A. Blake, K. V. L. N. Sastry, and F. C. De Lucia, J. Chem. Phys. **80**, 95 (1984).
[39] See EPAPS Document No. E-JCPSA6-127-008727 for HCO fragment (N, K_a) state distributions following the excitation of H_2CO to 19 different rotational lines between 31 518 and 31 815 cm^{-1}. This document can be reached via a direct link in the online article's HTML reference section or via the EPAPS homepage (http://www.aip.org/pubservs/epaps.html).
[40] G. Herzberg, *Electronic Spectra of Polyatomic Molecules*, Molecular Structure and Molecular Spectra Vol. III (Van Nostrand, Princeton, NJ, 1966).
[41] C. G. Stevens and J. C. D. Brand, J. Chem. Phys. **58**, 3324 (1973).
[42] C. G. Stevens and J. C. D. Brand, J. Chem. Phys. **58**, 3331 (1973).
[43] D. A. Ramsay and S. M. Till, Can. J. Phys. **57**, 1224 (1979).
[44] C. M. L. Kerr, D. C. Moule, and D. A. Ramsay, Can. J. Phys. **61**, 6 (1982).
[45] P. J. Bruna, R. J. Buenker, and S. D. Peyerimhoff, J. Mol. Struct. **32**, 217 (1976).
[46] A. D. Sappey and D. R. Crosley, J. Chem. Phys. **93**, 7601 (1990).
[47] J. A. Logan, M. J. Prather, S. C. Wofsy, and M. B. McElroy, J. Geophys. Res. **86**, 7210 (1981).
[48] S. P. Sander, R. R. Friedl, A. R. Ravishankara *et al.*, *Chemical Kinetics and Photochemical Data for Use in Atmospheric Studies*, Jet Propulsion Laboratory, California Institute of Technology, Evaluation Mo. 14, JPL Publ. 02-25, 2003 (http://jpldataeval.jpl.nasa.gov/).
[49] A. Horowitz and J. G. Calvert, Int. J. Chem. Kinet. **10**, 713 (1978).
[50] J. H. Clark, C. B. Moore, and N. S. Nogar, J. Chem. Phys. **68**, 1264 (1978).
[51] K. Y. Tang, P. W. Fairchild, and E. K. C. Lee, J. Phys. Chem. **83**, 569 (1979).
[52] G. K. Moortgat, W. Seiler, and P. Warneck, J. Chem. Phys. **78**, 1185 (1983).
[53] G. D. Smith, L. T. Molina, and M. J. Molina, J. Phys. Chem. A **106**, 1233 (2002).
[54] F. D. Pope, C. A. Smith, P. R. Davis, D. E. Shallcross, M. N. R. Ashfold, and A. J. Orr-Ewing, Faraday Discuss. **130**, 59 (2005).
[55] P. Ho, D. J. Bamford, R. J. Buss, Y. T. Lee, and C. B. Moore, J. Chem. Phys. **76**, 3630 (1982).
[56] M. Tulej, G. Knopp, P. Beaud, T. Gerber, and P. P. Radi, J. Raman Spectrosc. **36**, 109 (2005).
[57] H.-M. Yin, S. J. Rowling, A. Büll, and S. H. Kable, J. Chem. Phys. **127**, 064302 (2007), following paper.
[58] C. L. Reed, Ph.D. thesis, University of Bristol, 1997.
[59] P. A. Cook, Ph.D. thesis, University of Bristol, 2001.
[60] R. H. Qadiri, Ph.D. thesis, University of Bristol, 2004.